Letters

A Single-Switch and Parameter-Insensitive Capacitive Power Transfer System for Biomedical Implants

Dingyuan Tang, Wei Zhou, *Senior Member, IEEE*, Feng Xiao, Yifei Zhang, Zhaotian Yan, *Member, IEEE*, Ruikun Mai, *Senior Member, IEEE*, and Zhengyou He, *Senior Member, IEEE*

***Abstract*—This letter proposes a nonresonant capacitive power transfer system for active biomedical implants that eliminates resonance dependency while maintaining physical isolation. By leveraging biological tissue as the dielectric medium in a four-plate coupler and drawing inspiration from Zeta converter topology, the system achieves parameter insensitivity and single-switch control. Theoretical analysis via state-space averaging confirms output voltage regulation solely through duty-cycle adjustment, independent of component variations. Experimental validation using 20 mm × 20 mm plates through 4-mm pigskin demonstrates 207 mW power transfer with 30.1% efficiency at 1 MHz with a simplified receiver circuit (1 diode/1 inductor/1 capacitor). The system maintains 3.7 V output under 150% load transients, 100% inductance variations, fat content change and issue bending.**

***Index Terms*—Active biomedical implants (ABIs), capacitive power transfer (CPT), parameter-insensitive, single-switch, zeta converter.**

I. Introduction

IN RECENT years, Active Biomedical Implants (ABIs) such as pacemakers, artificial hip joints, and cochlear implants have become increasingly common in medical diagnosis and treatment. Currently, ABIs typically draw power from either built-in lithium batteries or transcutaneous wires. However, batteries have limited lifespans (typically 3–8 years), necessitating surgical replacement. This causes patient discomfort and poses a risk of electrolyte leakage that may harm surrounding tissue. Transcutaneous wires create a permanent opening, posing infection risks, and restricting patient mobility.

Received 17 July 2025; revised 15 September 2025; accepted 8 October 2025. Date of publication 10 October 2025; date of current version 13 November 2025. This work was supported in part by Sichuan Science and Technology Program under Grant 2025ZNSFSC1239 and in part by the Fundamental Research Funds for the Central Universities under Grant 2682025ZTPY046. *(Corresponding author: Wei Zhou.)*

Dingyuan Tang, Wei Zhou, Feng Xiao, Yifei Zhang, Ruikun Mai, and Zhengyou He are with the School of Electrical Engineering, Southwest Jiaotong University, Chengdu 611756, China (e-mail: tdy@my.swjtu.edu.cn; wzhou@swjtu.edu.cn; xfqaq@my.swjtu.edu.cn; 2024210709@my.swjtu.edu.cn; mairk@swjtu.edu.cn; hezy@swjtu.edu.cn).

Zhaotian Yan is with the School of Electrical Engineering, Hong Kong University of Science and Technology, Hong Kong SAR 999077, China (e-mail: yanzhaotian@ust.hk).

Color versions of one or more figures in this article are available at https://doi.org/10.1109/TPEL.2025.3620358.

Digital Object Identifier 10.1109/TPEL.2025.3620358

Wireless Power Transfer (WPT) enables power transmission without physical electrical contact, serving as an effective solution for ABI charging [1]. Capacitive Power Transfer (CPT) is a WPT technique based on electric field coupling, offering key advantages for ABIs: minimizing EMI and eddy current losses, thus reducing tissue heating risks and meeting SAR safety limits. Crucially, CPT performance is unaffected by nearby metal implants (e.g., pacemakers). Ferromagnetic core-free coupling plates reduce system size/weight, facilitate flexible substrate integration, and support ABI miniaturization [2]. While CPT shows promise for ABI charging, key challenges persist: practical hurdles in ensuring accurate resonance [3] and ABI space constraints.

Existing studies have proposed nonresonant CPT systems without inductor compensation. Such systems typically operate at relatively high frequencies ($>$ 100 MHz) [4] to reduce loop impedance. However, limited by the voltage and current withstand capabilities of high-frequency semiconductor devices, their transmitted power is often restricted to the tens-of-milliwatt level [5]. Another category of nonresonant CPT systems operates at lower frequencies, but their power level also remains hard to enhance due to large loop impedance [6]. Most existing CPT systems for ABIs adopt resonant topologies [7] and demonstrates promising performance under idealized laboratory conditions their practical deployment in ABIs charging scenarios faces significant challenges.The primary difficulties arise from two factors: 1) variations in the biological tissues, such as changes in body composition, alter the coupling parameters and consequently impair the resonant behavior of the system [8] and 2) component parameters, such as those of compensation inductors or capacitors, are susceptible to thermal drift and manufacturing tolerances, further exacerbating system detuning. To address these challenges, dynamic tuning control presents a potential solution. In [9], automatic frequency calibration enables adaptive tuning to counteract detuning induced by parameter variations. However, the practical implementation of this approach requires complex detection.

ABI require compact dc power supplies for battery charging, yet its implanted receivers face severe space constraints. Conventional approaches adopt bridge rectifiers, necessitating bulky discrete components: half-bridge configurations require two diodes plus filtering circuits, while full-bridge designs

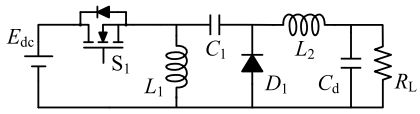

Fig. 1. Conventional Zeta converter.

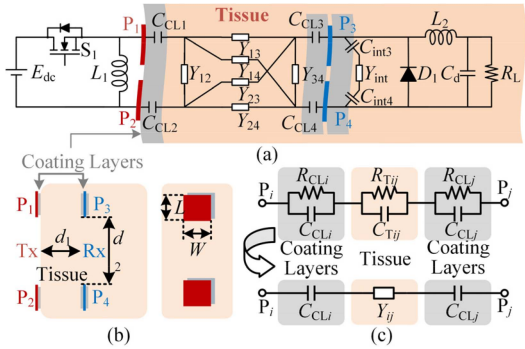

Fig. 2. The proposed CPT system for ABIs. (a) Overall circuit, (b) coupler dimensions, and (c) coupling parameters.

demand four diodes with additional passive filters [9], [10]. These solutions significantly hinder device miniaturization due to excessive space occupation by diodes and filtering capacitors. Furthermore, if the output voltage regulation is infeasible via the external transmitter, a dc–dc converter [11] must be integrated into the implanted module, further increasing the system volume and contradicting the minimalistic design imperative for implantable systems.

This letter proposes a novel nonresonant CPT system with single-switch control and parameter insensitivity. Compared with existing nonresonant systems, the proposed system still uses inductors but achieves a significant improvement in transmitted power. While matching the power level of resonant CPT systems, it obviates the need for resonance between the inductor and self-capacitor. The system has a simple structure, fewer components, and a quasi-Zeta converter topology. Enabling output voltage regulation via simple duty cycle adjustment, it delivers excellent adaptability to biological tissue load variations. The main contributions of this letter are as follows:

1) Establishing a four-plate time-domain model with biological tissue as the medium, and proposing a novel CPT architecture integrating this model with Zeta circuits.
2) Analyzing the operating modes of the proposed CPT system, establishing its model via the State-Space Averaging (SSA) method, and demonstrating the insensitivity of the system output voltage to component parameters.

II. Capacitive Coupling Model Considering Tissue

Fig. 1 shows the circuit of the conventional Zeta converter and the CPT system based on it. In the conventional Zeta circuit, the topology is divided into two parts by the lumped capacitor C_1. Thus, it is theoretically feasible to achieve physical isolation between the source-side circuit and the load circuit by replacing C_1 with four coupling plates.

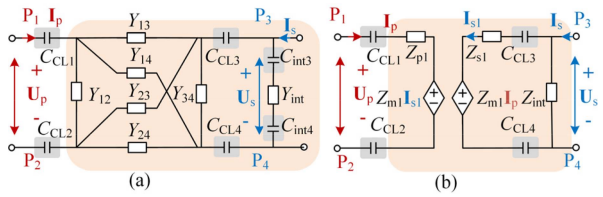

Fig. 3. Capacitive coupler (a) seven-admittance equivalent circuit and (b) series-connected equivalent circuit.

The proposed CPT system is shown in Fig. 2(a), the capacitive coupler consists of four coupling plates (P_1∼P_4). Specifically, two receiving plates are placed between the skin and subcutaneous tissue, with a 1 μm Parylene-N layer against the skin and a 0.15 mm Kapton layer against the fat. Both films prevent direct conduction current generation in the tissue. As marked in Fig. 2(b), the length and width of the plates are L and W. The skin thickness is d_1, and the spacing between the plates is d_2.

The equivalent circuit between any two plates P_i and P_j (i, $j \le 4$, $i, j \in \mathbf{N}^+$ and $i \neq j$) is shown in Fig. 2(b). Both the coating and the tissue can be equivalent to a parallel R–C circuit as shown in Fig. 2(c). The impedance between plate P_i (or j) and the tissue through the coating is parallel combination of $R_{\mathrm{CL}\ i\ (\mathrm{or}\ j)}$ and $C_{\mathrm{CL}\ i\ (\mathrm{or}\ j)}$. Noted that high-quality coatings provide good insulation: R_{CL} value is very large, so only C_{CL} is considered. The equivalent capacitance C_{CL} of the coating layer can be directly measured by measuring the capacitance between the coated and uncoated plates. Similarly, the impedance between P_i and P_j through the tissue is a parallel combination of $R_{\mathrm{T}\ ij}$ and $C_{\mathrm{T}\ ij}$, equivalently represented as admittance Y_{ij}. In addition, considering tissue influence on receiver plate backs, two film capacitances for the Kapton coating on P_3/P_4 backs are defined as C_{int3} and C_{int4}. Furthermore, Y_{int} is defined as the tissue admittance between P_3/P_4 backs. Admittances Y_{ij} and Y_{int} are obtained via Maxwell simulations.

The port voltages and currents of the coupler are $\mathbf{U}_{\mathrm{p}}$, $\mathbf{U}_{\mathrm{s}}$, $\mathbf{I}_{\mathrm{p}}$, and $\mathbf{I}_{\mathrm{s}}$. The seven-admittance equivalent circuit in Fig. 3(a) can be further equivalent to the circuit in Fig. 3(b), consisting of a series-connected self-impedance and a voltage controlled current source (VCCS). The equivalent-circuit derivation process is detailed in [12]. The parameter relationships between the two equivalent circuits in Fig. 3 are given by the following:

$$\begin{cases} Z_{\mathrm{p}} = \frac{Y_{\mathrm{s}}}{Y_{\mathrm{p}}Y_{\mathrm{s}}-Y_{\mathrm{m}}{}^2} \\ Z_{\mathrm{s}} = \frac{Y_{\mathrm{p}}}{Y_{\mathrm{p}}Y_{\mathrm{s}}-Y_{\mathrm{m}}{}^2} \\ Z_{\mathrm{m}} = \frac{-Y_{\mathrm{m}}}{Y_{\mathrm{p}}Y_{\mathrm{s}}-Y_{\mathrm{m}}{}^2} \end{cases} \text{and} \quad \begin{cases} Z_{\mathrm{int}} = \frac{1}{Y_{\mathrm{int}}} + \frac{C_{\mathrm{int3}}+C_{\mathrm{int4}}}{j\omega C_{\mathrm{int3}}C_{\mathrm{int4}}} \\ Z_{\mathrm{CLp}} = \frac{C_{\mathrm{CL1}}+C_{\mathrm{CL2}}}{j\omega C_{\mathrm{CL1}}C_{\mathrm{CL2}}} \\ Z_{\mathrm{CLs}} = \frac{C_{\mathrm{CL3}}+C_{\mathrm{CL4}}}{j\omega C_{\mathrm{CL3}}C_{\mathrm{CL4}}} \end{cases} \tag{1}$$

$$\begin{cases} Y_{\mathrm{p}} = Y_{12} + \frac{(Y_{13}+Y_{14})(Y_{23}+Y_{24})}{Y_{13}+Y_{14}+Y_{23}+Y_{24}} \\ Y_{\mathrm{s}} = Y_{34} + \frac{(Y_{13}+Y_{23})(Y_{14}+Y_{24})}{Y_{13}+Y_{14}+Y_{23}+Y_{24}} \\ Y_{\mathrm{m}} = \frac{Y_{13}Y_{24}-Y_{14}Y_{23}}{Y_{13}+Y_{14}+Y_{23}+Y_{24}} \end{cases} . \tag{2}$$

According to Kirchhoff's Current Law (KCL), the current $\mathbf{I}_{\mathrm{s1}}$ in Fig. 3(b) can be expressed as follows:

$$\mathbf{I}_{\mathrm{s1}} = \frac{Z_{\mathrm{in}}}{(Z_{\mathrm{s1}}+Z_{\mathrm{CLs}})+Z_{\mathrm{in}}} \cdot \mathbf{I}_{\mathrm{s}} - \frac{Z_{\mathrm{m1}}}{(Z_{\mathrm{s1}}+Z_{\mathrm{CLs}})+Z_{\mathrm{in}}} \cdot \mathbf{I}_{\mathrm{p}}. \tag{3}$$

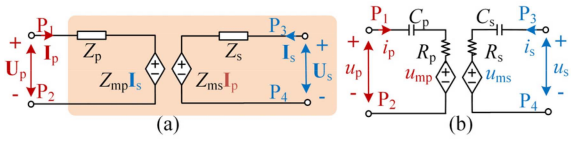

Fig. 4. Series-connected equivalent circuit of the coupler in (a) frequency-domain and (b) time domain.

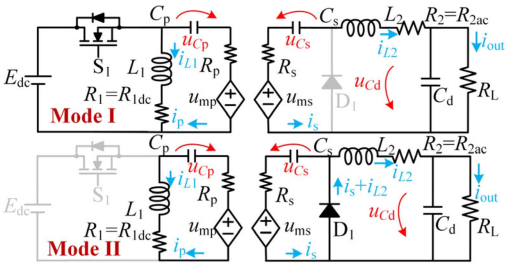

Fig. 5. The proposed CPT system and its working mode I and mode II.

According to Fig. 3(b) and (3), Fig. 3(b) can be further simplified as Fig. 4(a), which satisfies (4)

$$\begin{cases} \mathbf{U}_{\mathrm{p}} = \underbrace{\left(Z_{\mathrm{p1}} + Z_{\mathrm{CLp}} - \frac{Z_{\mathrm{m1}}^2}{Z_{\mathrm{s1}}+Z_{\mathrm{CLs}}+Z_{\mathrm{int}}}\right)}_{Z_{\mathrm{p}}} \cdot \mathbf{I}_{\mathrm{p}} \\ \quad + \underbrace{\frac{Z_{\mathrm{m1}} Z_{\mathrm{int}}}{Z_{\mathrm{s1}}+Z_{\mathrm{CLs}}+Z_{\mathrm{int}}}}_{Z_{\mathrm{mp}}} \cdot \mathbf{I}_{\mathrm{s}} \\ \mathbf{U}_{\mathrm{s}} = \underbrace{\frac{(Z_{\mathrm{s1}}+Z_{\mathrm{CLs}})Z_{\mathrm{int}}}{Z_{\mathrm{s1}}+Z_{\mathrm{CLs}}+Z_{\mathrm{int}}}}_{Z_{\mathrm{s}}} \cdot \mathbf{I}_{\mathrm{s}} + \underbrace{\left(Z_{\mathrm{m1}} - \frac{(Z_{\mathrm{s1}}+Z_{\mathrm{CLs}})Z_{\mathrm{m1}}}{Z_{\mathrm{s1}}+Z_{\mathrm{CLs}}+Z_{\mathrm{int}}}\right)}_{Z_{\mathrm{ms}}} \cdot \mathbf{I}_{\mathrm{p}} \end{cases}. \quad (4)$$

The impedance Z_{p}, Z_{s}, Z_{mp}, and Z_{ms} in Fig. 4(a) are series of equivalent R–C pairs, satisfying $Z_{\mathrm{p}} = R_{\mathrm{p}} + 1/(j\omega C_{\mathrm{p}})$, $Z_{\mathrm{s}} = R_{\mathrm{s}} + 1/(j\omega C_{\mathrm{s}})$, and $Z_{\mathrm{mp,s}} = R_{\mathrm{mp,s}} + 1/(j\omega C_{\mathrm{mp,s}})$. The time-domain model for the frequency-domain model in Fig. 4(a) is shown in Fig. 4(b). The equivalent capacitance and sources u_{mp}, u_{ms} in Fig. 4(b) are as follows:

$$\begin{cases} C_{\mathrm{p}} = -\frac{1}{2\pi f \mathrm{Im}\{Z_{\mathrm{p}}\}} \\ C_{\mathrm{s}} = -\frac{1}{2\pi f \mathrm{Im}\{Z_{\mathrm{s}}\}} \end{cases} \text{and} \quad \begin{cases} u_{\mathrm{mp}} = R_{\mathrm{mp}} i_{\mathrm{s}} + \frac{C_{\mathrm{s}}}{C_{\mathrm{mp}}} u_{C\mathrm{s}} \\ u_{\mathrm{ms}} = R_{\mathrm{ms}} i_{\mathrm{p}} + \frac{C_{\mathrm{p}}}{C_{\mathrm{ms}}} u_{C\mathrm{p}} \end{cases}. \quad (5)$$

III. Working Principle of the System

Compared with conventional air-gap CPT systems, the main coupling capacitances of the coupler for tissues reaches tens of nano-farads, which is significantly larger than that of the former. Consequently, similar to capacitive dc–dc converters [13], the system state variables (e.g., inductor currents and capacitor voltages) are dominated by dc components, with ripple amplitudes substantially smaller than their dc offsets. This characteristic eliminates the need for resonant compensation and enables modeling the system via the SSA method.

The CPT system operates in two modes as shown in Fig. 5.

1) *Mode I:* When switch S_1 is turned ON, inductor L_1 stores energy, diode D_1 remains OFF, and power is delivered to the load R_{L} through the path C_{p}-u_{m}-C_{s}-L_2.

TABLE I
System Main Parameters

Para.	Val.	Para.	Val.	Para.	Val.
R_{p}	273.0 Ω	C_{p}	1.12 nF	$C_{\mathrm{CL1-4}}$	16.0 nF
R_{s}	265.1 Ω	C_{s}	1.11 nF	R_{L}	0~250 Ω
R_{ms}, R_{mp}	242.2 Ω	C_{ms}, C_{mp}	1.45 nF	W, L	20 mm
d_1	50 mm	d_2	4 mm	f	1 MHz
$C_{\mathrm{Clint3,4}}$	106.7 pF	R_{1dc}	0.2 Ω	R_{2dc}	1.1 Ω
E_{dc}	9 V	R_{1ac}	8.2 Ω	R_{2ac}	18 Ω

2) *Mode II:* When switch S_1 is turned OFF, L_1 continues conducting and transfers power to C_{p} and C_{s}, while inductor L_2 supplies R_{L} through D_1.

Select the currents i_{L1}, i_{L2}, and voltages $u_{C\mathrm{p}}$, $u_{C\mathrm{s}}$, and $u_{C\mathrm{d}}$ as state variables. The output voltage is derived using the SSA method. The system operating states and output equation are given by (4)

$$\begin{cases} \frac{\mathrm{d}x_{\mathrm{n}}(t)}{\mathrm{d}t} = \mathbf{A} \cdot x_n(t) + \mathbf{B} \cdot E_{\mathrm{dc}} \\ u_{\mathrm{out}} = \mathbf{C} \cdot x_n(t) + \mathbf{E} \cdot E_{\mathrm{dc}} \end{cases} \quad (6)$$

where $x_n(t) = [u_{C\mathrm{p}}, u_{C\mathrm{s}}, i_{L1}, i_{L2}, u_{C\mathrm{d}}]^{\mathrm{T}}$.

Matrices $\mathbf{A}$ and $\mathbf{B}$ are constructed from submatrices $\mathbf{A}_1$, $\mathbf{A}_2$ and $\mathbf{B}_1$, $\mathbf{B}_2$, respectively, corresponding to the two operational modes of the system. Assuming the duty cycle of the driving signal for switch S_1 is D, the state-space matrices are defined as

$$\begin{cases} \mathbf{A} = D \cdot \mathbf{A}_1 + (1-D) \cdot \mathbf{A}_2 \\ \mathbf{B} = D \cdot \mathbf{B}_1 + (1-D) \cdot \mathbf{B}_2 \end{cases}. \quad (7)$$

The explicit forms of $\mathbf{A}_1$, $\mathbf{A}_2$, $\mathbf{B}_1$, and $\mathbf{B}_2$ are given in (8) and (9) shown at the bottom of this next page.

By solving (7), it can be derived

$$\begin{bmatrix} \bar{u}_{C\mathrm{p}} & \bar{u}_{C\mathrm{s}} & \bar{i}_{L1} & \bar{i}_{L2} & \bar{u}_{C\mathrm{d}} \end{bmatrix}^{\mathrm{T}} = -\mathbf{A}^{-1}\mathbf{B} \cdot E_{\mathrm{dc}}. \quad (10)$$

The output voltage u_{out} is

$$u_{\mathrm{out}} = \bar{u}_{C\mathrm{d}} = \frac{D(1-D) R_{\mathrm{ms}} R_L E_{\mathrm{dc}}}{\left\{ \begin{array}{c} R_{\mathrm{p}}(R_{\mathrm{L}}+R_2) + 2D^3 R_1 (R_2 + R_{\mathrm{L}} - R_{\mathrm{s}}) + \\ D^2 [R_{\mathrm{mp}} R_{\mathrm{ms}} + R_{\mathrm{p}}(R_2 + R_{\mathrm{L}} - R_{\mathrm{s}}) \\ + R_1(-3R_2 - 3R_{\mathrm{L}} + R_{\mathrm{s}})] \\ + D[R_1(R_2 + R_{\mathrm{L}}) - R_{\mathrm{ms}} R_{\mathrm{mp}} \\ + R_{\mathrm{p}}(-2R_2 - 2R_{\mathrm{L}} + R_{\mathrm{s}})] \end{array} \right\}}. \quad (11)$$

IV. System Design and Experimental Research

A. System Design

The experimental prototype is illustrated in Fig. 6. A 4-mm-thick pigskin tissue is used, coupled with four plates (20 mm × 20 mm) coated with 1-μm-thick Parylene-N and spaced 40 mm apart. The transmitting circuit is composed of a MOSFET S_1 and an inductor L_1, powered by a battery with voltage of 12 V. The receiving circuit has a reduced volume, consisting of surface mounted diode D_1, inductor L_2, and capacitor C_{d}. Table I shows the equivalent parameters of the experimental prototype.

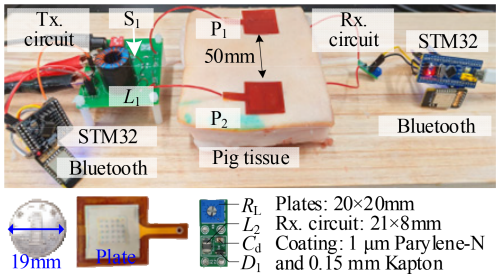

Fig. 6. Experimental prototype.

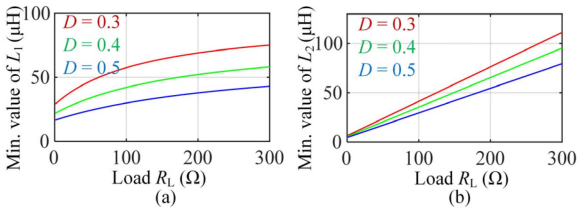

Fig. 7. Under open-loop conditions, the minimum values of (a) L_1 and (b) L_2.

For the inductors L_1 and L_2, the condition for continuous inductor current is that their peak-to-peak current ripples are less than twice their average currents, as shown in (12). Thus, the inductor values should satisfy (13). Specifically, the minimum values of L_1 and L_2 under different duty cycles in the open-loop operating condition are presented in Fig. 7

$$\begin{cases} \Delta i_{L1} = \frac{E_{\rm dc} DT}{L_1} \le 2\bar{i}_{L1} \\ \Delta i_{L2} = \frac{u_{\rm out}(R_{2\rm ac}+R_{\rm L})(1-D)T}{L_2 R_{\rm L}} \le 2i_{\rm out} = \frac{2u_{\rm out}}{R_{\rm L}} \end{cases} \tag{12}$$

$$\begin{cases} L_1 \ge \frac{E_{\rm dc} DT}{2\bar{i}_{L1}} \\ L_2 \ge \frac{1}{2}\left(R_{\rm L}+R_{2\rm ac}\right)(1-D)T \end{cases}. \tag{13}$$

In the proposed CPT system, it is sufficient for the values of inductors L_1 and L_2 to be larger than their minimum values to maintain the system's continuous current mode (CCM), without the need to maintain a resonant state. Based on the analysis, two standard inductors with $L_1 = 150\ \mu$H and $L_2 = 100\ \mu$H are selected. The effective load range is 0–250 Ω.

B. Open-Loop Characteristics

The losses of the system stem from the following five components: coupler loss $P_{\rm Coupler}$, switching loss $P_{\rm sw}$, loss of L_1 inductor $P_{\rm L1}$, loss of L_2 inductor $P_{\rm L2}$, and loss of D_1 diode $P_{\rm D1}$. Thus, the overall efficiency of the system can be expressed as follows:

$$\eta = \frac{P_{\rm out}}{P_{\rm out}+P_{\rm Coupler}+P_{L1}+P_{L2}+P_{\rm sw}+P_{D1}}. \tag{14}$$

Each power losses of the system is evaluated by (15)

$$\begin{cases} P_{\rm out} = u_{\rm out}^2 / R_{\rm L} \\ P_{\rm Coupler} = E_{\rm dc} D\left(\bar{i}_{\rm p1}+\bar{i}_{L1}\right) - \bar{i}_{L1}^2 R_{1\rm dc} - \bar{i}_{L2}^2 R_{2\rm ac} - P_{\rm out} \\ P_{\rm sw} = \frac{1}{2} E_{\rm dc}\left(\bar{i}_{\rm p1}+\bar{i}_{L1}\right)\left(t_{\rm r}+t_{\rm f}\right) f \\ P_{L1} = \bar{i}_{L1}^2 R_{1\rm dc} + \left(\frac{2\sqrt{2}\Delta i_{L1}}{\pi^2}\right)^2 R_{1\rm ac} \\ P_{L2} = \bar{i}_{L2}^2 R_{2\rm dc} + \left(\frac{2\sqrt{2}\Delta i_{L2}}{\pi^2}\right)^2 R_{2\rm ac} \\ P_{\rm D1} = \Delta U_{\rm D1}\left(\bar{i}_{\rm s2}+\bar{i}_{L2}\right)(1-D) \end{cases}. \tag{15}$$

Among these parameters, $\bar{i}_{\rm L1}$ and $\bar{i}_{\rm L2}$ are the average currents of inductors L_1 and L_2 over the full cycle; f denotes the frequency, with a period of $T = 1/f$; $t_{\rm r}$ and $t_{\rm f}$ represent the turn-ON and turn-OFF times of the switch, where $t_{\rm r}+t_{\rm f} = 0.08T$; Δi_{L1} and Δi_{L2} are the peak-to-peak current ripples of inductors L_1 and L_2; $R_{1\rm dc}$ and $R_{1\rm ac}$ are the dc and ac internal resistances of L_1, while $R_{2\rm dc}$ and $R_{2\rm ac}$ are the dc and ac internal resistances of L_2; and $\Delta U_{D1} = 0.2$ V is the forward voltage drop of D_1. Let $\bar{i}_{\rm p1,2}$ and $\bar{i}_{\rm s1,2}$ denote the average currents of the power transmitter and receiver in Mode I and II, respectively. In Mode I, $\bar{i}_{\rm p1}$ and $\bar{i}_{\rm s1}$ satisfy (16)

$$\begin{cases} \bar{i}_{\rm p1} = \frac{u_{\rm ms}}{R_{\rm ms}} - \frac{C_{\rm p}}{C_{\rm ms} R_{\rm ms}} \bar{u}_{C\rm p} \\ \bar{i}_{\rm s1} = -\bar{i}_{L2} \end{cases}. \tag{16}$$

Based on volt–second balance of L_2, it can be obtained that

$$\left(u_{\rm ms} - R_{\rm s} i_{L2} + \bar{u}_{C\rm s} - \frac{R_{\rm L}+R_{2\rm ac}}{R_{\rm L}} \bar{u}_{C\rm d}\right)$$

$$\mathbf{A}_1 = \begin{bmatrix} -\frac{1}{C_{\rm p} R_{\rm p}} & -\frac{C_{\rm s}}{C_{\rm p} C_{\rm mp} R_{\rm p}} & 0 & \frac{R_{\rm mp}}{C_{\rm p} R_{\rm p}} & 0 \\ 0 & 0 & 0 & -\frac{1}{C_{\rm s}} & 0 \\ 0 & 0 & \frac{R_1}{L_2} & 0 & 0 \\ \frac{C_{\rm p}}{L_2 C_{\rm ms}} - \frac{R_{\rm ms}}{R_{\rm p} L_2} & \frac{1}{L_2} - \frac{C_{\rm s} R_{\rm ms}}{R_{\rm p} L_2 C_{\rm mp}} & 0 & \frac{R_{\rm mp} R_{\rm ms}}{R_{\rm p} L_2} - \frac{(R_{\rm s}+R_2)}{L_2} & -\frac{1}{L_2} \\ 0 & 0 & 0 & \frac{1}{C_{\rm d}} & -\frac{1}{C_{\rm d} R_{\rm L}} \end{bmatrix}, \mathbf{B}_1 = \begin{bmatrix} \frac{1}{C_{\rm p} R_{\rm p}} \\ 0 \\ \frac{1}{L_1} \\ \frac{R_{\rm m}}{R_{\rm p} L_2} \\ 0 \end{bmatrix}. \tag{8}$$

$$\mathbf{A}_2 = \begin{bmatrix} 0 & 0 & -\frac{1}{C_{\rm p}} & 0 & 0 \\ -\frac{C_{\rm p}}{C_{\rm s} R_{\rm s} C_{\rm ms}} & -\frac{1}{C_{\rm s} R_{\rm s}} & \frac{R_{\rm ms}}{C_{\rm s} R_{\rm s}} & 0 & 0 \\ \frac{1}{L_1} - \frac{C_{\rm p} R_{\rm mp}}{R_{\rm s} L_1 C_{\rm mp}} & \frac{C_{\rm s}}{L_1 C_{\rm mp}} - \frac{R_{\rm mp}}{R_{\rm s} L_1} & \frac{R_{\rm mp} R_{\rm ms}}{R_{\rm s} L_1} - \frac{R_1+R_{\rm p}}{L_1} & 0 & 0 \\ 0 & 0 & 0 & -\frac{R_2}{L_2} & -\frac{1}{L_2} \\ 0 & 0 & 0 & \frac{1}{C_{\rm d}} & -\frac{1}{C_{\rm d} R_{\rm L}} \end{bmatrix}, \mathbf{B}_2 = \begin{bmatrix} 0 \\ 0 \\ 0 \\ 0 \\ 0 \end{bmatrix}. \tag{9}$$

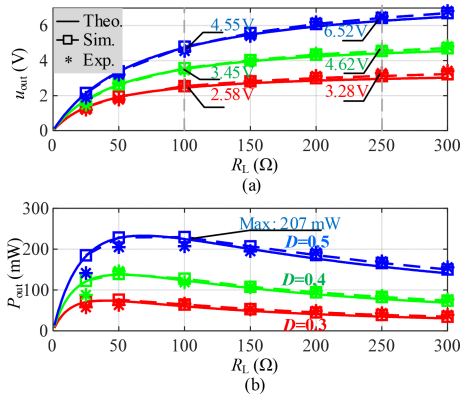

Fig. 8. System output curves against the load resistance. (a) u_{out} and (b) P_{out}.

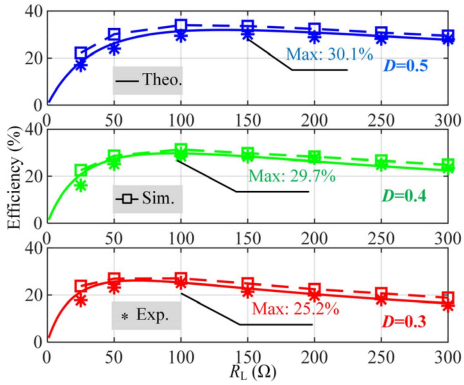

Fig. 9. PTE curves against the load resistance.

$$D = \frac{R_{\mathrm{L}}+R_{2\mathrm{ac}}}{R_{\mathrm{L}}}(1-D)\,\bar{u}_{C\mathrm{d}}. \tag{17}$$

Combining (5) and (17), the solution is obtained as follows:

$$\bar{i}_{\mathrm{p1}} = \frac{R_{\mathrm{L}}+R_{2\mathrm{ac}}}{DR_{\mathrm{L}}R_{\mathrm{ms}}}\bar{u}_{C\mathrm{d}} + \frac{R_{\mathrm{s}}}{R_{\mathrm{ms}}}\bar{i}_{L2} - \frac{\bar{u}_{C\mathrm{s}}}{R_{\mathrm{ms}}} - \frac{C_{\mathrm{p}}}{C_{\mathrm{ms}}R_{\mathrm{ms}}}\bar{u}_{C\mathrm{p}}. \tag{18}$$

Similarly, in Mode II

$$\begin{cases} \bar{i}_{\mathrm{p2}} = -\bar{i}_{L1} \\ \bar{i}_{\mathrm{s2}} = \dfrac{u_{\mathrm{mp}}}{R_{\mathrm{mp}}} - \dfrac{C_{\mathrm{s}}}{C_{\mathrm{mp}}R_{\mathrm{mp}}}\bar{u}_{C\mathrm{s}} \end{cases}. \tag{19}$$

From the volt–second balance of inductor L_1, it can be obtained that

$$E_{\mathrm{dc}}D = (u_{\mathrm{mp}} - R_{\mathrm{p}}\bar{i}_{L1} + \bar{u}_{C\mathrm{p}})(1-D). \tag{20}$$

Combining (5) and (20), the solution is obtained as follows:

$$\bar{i}_{\mathrm{s2}} = \frac{E_{\mathrm{dc}}D}{(1-D)R_{\mathrm{mp}}} + \frac{R_{\mathrm{p}}\bar{i}_{L1}}{R_{\mathrm{mp}}} - \frac{\bar{u}_{C\mathrm{p}}}{R_{\mathrm{mp}}} - \frac{C_{\mathrm{s}}}{C_{\mathrm{m}}R_{\mathrm{m}}}\bar{u}_{C\mathrm{s}}. \tag{21}$$

Based on the above analysis, the theoretical losses of each part of the system can be calculated. Figs. 8 and 9 present the comparison of the curves of the system's output voltage, power delivery level (PDL), and power transfer efficiency (PTE) versus load resistance in the open-loop state. From the curve comparison, it can be observed that the theoretical, simulation, and the measured results are basically consistent.

Taking $D = 0.4$ as an example, the system's PTE reaches a peak value of 29.7% when the load resistance is 90 Ω. Under this state, theoretical calculations are performed on the losses of each part of the system, and the results are as shown in Fig. 10. It

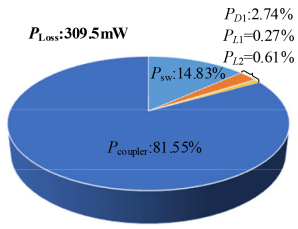

Fig. 10. Loss distribution of the system under $D = 0.4$ and optimal efficiency.

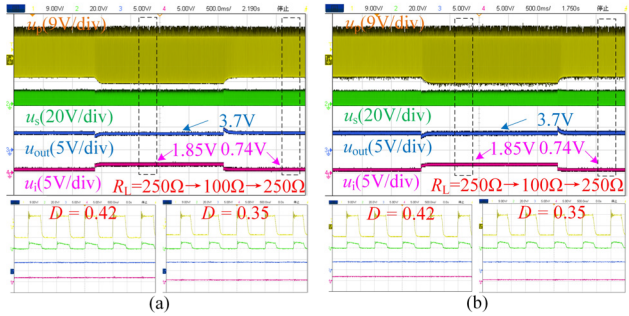

Fig. 11. System waveforms during load switching in (a) Case I and (b) Case II.

shows that the total loss of the system is 309.5 mW, among which the coupler loss accounts for as high as 81.55% , followed by the switching loss with a proportion of 14.83% , and the losses of the remaining parts are relatively small.

C. Closed-Loop Control and Parameter Insensitivity

To further validate the practical value of the proposed system, a closed-loop control experiment was conducted. The output voltage reference was specified as 3.7 V, a common battery voltage. Two cases were tested: Case-I used $L_1 = 150$ μH and $L_2 = 100$ μH, while Case-II used $L_1 = 75$ μH and $L_2 = 200$ μH. For both cases, the load was switched from 250 Ω to 100 Ω and then returned to 250 Ω. The corresponding voltages u_{p}, u_{s}, u_{i}, and u_{out} are shown in Fig. 11. Note that u_{i} is the voltage across a constant resistor, which characterizes load current variations.

Two experiments are conducted to verify the system's insensitivity to variations in coupling conditions. In Case-III, a 0.5-mm fat is placed between the receiver plates and the skin to simulate the impact of changes in fat content. In Case-IV, the tissue is bended inward by 30° to simulate the impact of patient posture changes on the system. The results are shown in Fig. 12.

Fig. 11 demonstrates that doubling the system inductances resulted in operating characteristics and waveforms exhibiting close resemblance. In addition, Fig. 12 verifies that increases in fat content and tissue bending do not exert excessive influence on the system. Crucially, in all four cases, the target 3.7 V output voltage was achieved at approximately the same duty cycle. This experiment confirms the feasibility of regulating the output voltage through the duty cycle of a single switch and establishes the system's insensitivity to component variations.

D. Comparison With Existing Literatures

As compared in Table II, the proposed system achieves significant implementation advantages. Crucially, the receiver

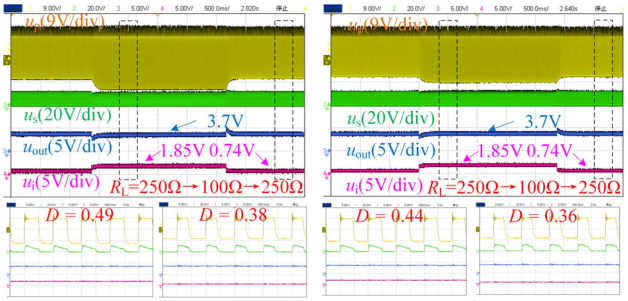

Fig. 12. System waveforms during load switching in (a) Case III and (b) Case IV.

TABLE II
COMPARISONS BETWEEN RECENT WORKS

Type	Ref.	Tx.	Rx.	PTE/%	PDL/mW	*f*/MHz
Resonant CPT	[9]	2L	4D+1C	54 (DC-DC)	150	0.1~3.5
	[10]	1L	2D+1L+1C	31.3 (DC-DC)	200	1/2/5
	[11]	2L	2L+2C +1Chip	50.4 (Coupler)	232	1~10
Nonresonant CPT	[4]	None	2C+1D	2.2 (AC-DC)	22	1300
	[5]	None	1L+1C +1Chip	>10 (AC-DC)	>1	1000
	[6]	None	/	0.2 (AC-AC)	5.7	6.78
	This Work	1L	1D+1L+1C	30.1 (DC-DC)	207	1

Note: L-inductor, C-capacitor, S-switch, D-diode .

requires merely 1 diode, 1 inductor, and 1 capacitor, demonstrating superior component economy and compact design. Furthermore, compared with resonant CPT systems, the proposed system exhibits lower parameter sensitivity; compared with nonresonant CPT systems, it achieves higher PDL and PTE.

V. CONCLUSION

This letter demonstrated a nonresonant CPT system for ABIs, achieving 207 mW PDL and 30.1% PTE through 4 mm biological tissue at 1 MHz using a single-switch transmitter and ultra-simplified receiver (1 diode/1 inductor/1 capacitor). Experiments confirm robust output regulation at 3.7 V under 150% load transients, 100% inductance variations, fat content variation and tissue bending, eliminating sensitivity to the parameter variation while reducing component count significantly, establishing a hardware-efficient solution for implantable applications.

REFERENCES

[1] Y. Liu, Y. Yao, and W.-H. Ki, "A 13.56-MHz single-input dual-output wireless power and data transfer system for bio-implants," *IEEE J. Solid-State Circuits*, vol. 59, no. 8, pp. 2557–2567, Aug. 2024.

[2] A. N. M. S. Hossain, P. Mohseni, and H. M. Lavasani, "Design and optimization of capacitive links for wireless power transfer to biomedical implants," *IEEE Trans. Biomed. Circuits Syst.*, vol. 16, no. 6, pp. 1299–1312, Dec. 2022.

[3] C. Han, S. Yu, Z. Zhang, and J. Mao, "An investigation of implantable capacitive coupling intra-body power transfer based on full-band loss compensation," *IEEE Trans. Power Electron.*, vol. 39, no. 7, pp. 8904–8915, Jul. 2024.

[4] A. Iqbal, A. Smida, M. Al-Hasan, I. Ben Mabrouk, and T. A. Denidni, "Highly isolated wireless power transfer and information co-delivery using a pacemaker duplex antenna," *IEEE Trans. Microw. Theory Techn.*, vol. 73, no. 2, pp. 1158–1170, Feb. 2025.

[5] A. I. Omi, A. Mukherjee, A. Jiang, and B. Chatterjee, "Towards battery-less internet of bodies: Energy harvester with reconfigurable stages enabled by galvanic body-coupled powering for bio-implants," in *Proc. IEEE Int. Symp. Circuits Syst.*, 2025, pp. 1–5.

[6] J. Minguillon et al., "Powering electronic implants by high frequency volume conduction: In human validation," *IEEE Trans. Biomed. Eng.*, vol. 70, no. 2, pp. 659–670, Feb. 2023.

[7] C. Cai et al., "Modeling and design of a transcutaneous resonant capacitive power transfer link for biomedical implants," *IEEE Trans. Power Electron.*, vol. 40, no. 2, pp. 3726–3737, Feb. 2025.

[8] A. N. M. S. Hossain, R. Erfani, P. Mohseni, and H. M. Lavasani, "On the non-idealities of a capacitive link for wireless power transfer to biomedical implants," *IEEE Trans. Biomed. Circuits Syst.*, vol. 15, no. 2, pp. 314–325, Apr. 2021.

[9] S. Nag, A. Koruprolu, S. M. Saikh, R. Erfani, and P. Mohseni, "Auto-resonant tuning for capacitive power and data telemetry using flexible patches," *IEEE Trans. Circuits Syst. II: Exp. Briefs*, vol. 67, no. 10, pp. 1804–1808, Oct. 2020.

[10] L. Yang et al., "Single wire capacitive wireless power transfer system for wearable biomedical sensors based on flexible graphene film material," *IEEE Trans. Biomed. Circuits Syst.*, vol. 16, no. 6, pp. 1337–1347, Dec. 2022.

[11] R. Erfani, F. Marefat, S. Nag, and P. Mohseni, "A 1–10-MHz frequency-aware CMOS active rectifier with dual-loop adaptive delay compensation and >230-mW output power for capacitively powered biomedical implants," *IEEE J. Solid-State Circuits*, vol. 55, no. 3, pp. 756–766, Mar. 2020.

[12] H. Zhang and F. Lu, "Insulated coupler structure design for the long-distance freshwater capacitive power transfer," *IEEE Trans. Ind. Informat.*, vol. 16, no. 8, pp. 5191–5201, Aug. 2020.

[13] A. Toebe, R. C. Beltrame, M. Mezaroba, A. L. Batschauer, and C. Rech, "Capacitive coupled step-down DC–DC converter with touch current limitation," *IEEE Trans. Power Electron.*, vol. 39, no. 8, pp. 9724–9735, Aug. 2024.